Numerical continuation of families of homoclinic connections of periodic orbits in the RTBP

E Barrabés[1], J M Mondelo[2] and M Ollé[3]

[1] Dept. Informàtica i Matemàtica Aplicada, Universitat de Girona, Avda. Lluís Santaló s/n, 17071 Girona, Spain

[2] IEEC & Dept. Matemàtiques. Universitat Autònoma de Barcelona, Edifici C, 08193 Bellaterra, Spain.

[3] Dept. de Matemàtica Aplicada I. Universitat Politècnica de Catalunya, Diagonal 647, 08028 Barcelona, Spain.

E-mail: barrabes@ima.udg.edu, jmm@mat.uab.cat, merce.olle@upc.edu

Abstract.
The goal of this paper is the numerical computation and continuation of homoclinic connections of the Lyapunov families of periodic orbits (p.o.) associated with the collinear equilibrium points, L_1, L_2, and L_3, of the planar circular Restricted Three–Body Problem (RTBP). We describe the method used that allows to follow individual families of homoclinic connections by numerical continuation of a system of (nonlinear) equations that has as unknowns the initial condition of the p.o., the linear approximation of its stable and unstable manifolds, and a point in a given Poincaré section in which the unstable and stable manifolds match. For the L_3 case, some comments are made on the geometry of the manifold tubes and the possibility of obtaining trajectories with prescribed itineraries.

AMS classification scheme numbers: 70F07, 70F15, 70H12, 70H33, 70K44

Submitted to: *Nonlinearity*

1. Introduction

Homoclinic and heteroclinic connections of hyperbolic invariant sets play an important role in the study of dynamical systems from a global point of view. Of special interest is their application to the design of space missions using libration point dynamics. Among the libration point missions up to present [10], Genesis [18] has been the first one to make use of a heteroclinic connection. The use of homoclinic and heteroclinic phenomena allows to envisage more complex missions, like low–energy transfers to the Moon [26] and the *Petit Grand Tour* to the moons of Jupiter [14]. Having as a goal the design of such complex missions in an automatic way, it is desirable to construct maps of homoclinic and heteroclinic connections in several primary–secondary systems. The methodology developed in this paper is mostly aimed at the construction of such maps.

For the design of such missions, the circular Restricted Three–Body Problem (RTBP) is the natural problem to start with. In the literature, attention is mostly focused on L_1 and L_2 because of its suitability to place permanent observatories of the Sun or of the whole celestial sphere [10]. The L_3 point has not been considered for astrodynamical applications, but horseshoe–type motion has drawn some attention from the astronomical point of view, as it is performed by co-orbital satellites of Saturn like Janus and Epimetheus [22], or by near Earth asteroids [9]. In [5], it is seen that the manifolds of both L_3 and its corresponding family of Lyapunov periodic orbits (LPO) play a role in this kind of motion.

Analytical proofs of the existence of homoclinic orbits to LPO around the L_1 and L_2 points have been given in [21, 23]. More recently, and by means of a computed assisted proof approach [28, 29], proofs of the existence of particularly shaped homoclinic and heteroclinic connections of Lyapunov orbits around L_1 and L_2 have been given.

From a numerical point of view, families of homoclinic and heteroclinic connections of both periodic orbits (p.o.) and 2D invariant tori in the L_1 and L_2 neighborhoods have been computed in the literature [6, 14, 15, 16, 20] by means of the use of semi-analytical techniques (asymptotic expansions with coefficients computed in finite–precision arithmetic). In these references, individual connections are found by matching the corresponding manifolds on a surface of section. Families are described by manually repeating this matching process for several values of a parameter, which is often the energy (or, equivalently, the Jacobi constant).

This paper is aimed at the numerical computation of families of homoclinic connections of p.o. The automation of the process just described was one of its main motivations. Another point we wanted to address is to overcome the (effective) convergence restrictions of semi–analytical procedures, which give very good approximations close to the libration points, but become unusable away from them. A final motivation for this paper is the exploration of the neighborhood of L_3, for which semi–analytical procedures do not give useful approximations.

We have used a method for the continuation of homoclinic connections that consists of raising a (nonlinear) system of equations whose solution is a curve that corresponds to a family of homoclinic connections. This system includes the equations of a p.o. in a Poincaré section, the eigenvalue/eigenvector equations for the linear approximation of the invariant manifolds of the p.o., and matching conditions for the manifolds on a second Poincaré section. The system of equations is numerically continued by a standard predictor-corrector method [2]. Both the system of equations and its differential with respect to the unknowns are evaluated by direct numerical integration of the differential equations, together with its first and second variational equations. For this, a variable step Runge–Kutta–Fehlberg method of orders 7 and 8 has been used with standard double–precision arithmetic. The instability due to the hyperbolic character of all the p.o. considered is coped with by a multiple shooting strategy.

The method just described has been applied to the continuation of families of transversal homoclinic connections of planar Lyapunov p.o. associated to the collinear

points of the planar, circular RTBP. For the L_1, L_2 case, the computations presented here are done for the Earth–Moon mass ratio, and can be considered an extension of the results of [6], both in the computation of new families and the continuation to higher energy levels. The computations for the L_3 case are new, and have been done for the Sun–Jupiter mass ratio in order to relate the results presented to previous works on horseshoe motion [4, 5].

Although the method presented here has only been applied to homoclinic connections of planar LPO of the RTBP, it can be used without modification to follow homoclinic connections of any family of p.o. of any Hamiltonian system.‡ Minor modifications would allow to follow heteroclinic connections of p.o. as well. It may also be generalized naturally to the continuation of connections of invariant tori, which will be the subject of future work.

A different approach to the continuation of homoclinic connections of p.o. can be found in [11], where the equations to solve are written in terms of boundary–value problems, in order to use the continuation package AUTO [12]. In the former reference, the continuation method proposed is applied to the the detection and continuation of a cycle-to-cycle connecting orbit in a food chain model.

The paper is structured as follows. Sect. 2 briefly recalls the circular, planar RTBP and describes the numerical method used for the continuation of families of homoclinic connections of p.o. Sect. 3 is devoted to numerical results, for L_1, L_2, in Sect. 3.1, and for L_3, in Sect. 3.2. For all three points, the main families of homoclinic connections are first systematically detected, in terms of the behavior of the manifold branches of the p.o., and then continued. For brevity, only primary homoclinics are considered in the L_1, L_2 cases. In the L_3 case, some comments are made on higher–order homoclinics and the possibility of generating trajectories with prescribed itineraries, using transit and non–transit trajectories as defined by Conley [8].

2. Homoclinic connections of Lyapunov p.o. of the RTBP

2.1. The circular, planar RTBP

The circular RTBP describes the motion of a particle of infinitesimal mass moving under the gravitational influence of two massive bodies, called primaries, that describe circular orbits around their common center of mass. We will consider the planar problem, in which the motion of the third body is contained in the plane of motion of the primaries. Taking a coordinate system that rotates with the primaries, with origin placed at their center of mass, and suitable units, we can assume that the primaries have masses $1-\mu$ and μ, $\mu \in (0, 1/2]$, their positions are fixed at $(\mu, 0)$ and $(\mu - 1, 0)$, and the period of their motions is 2π. With these assumptions, and introducing momenta $p_x = \dot{x} - y$ and $p_y = \dot{y} + x$, the equations of motion of the third body may be described by a Hamiltonian

‡ Actually, the method could work in any system in which a family of homoclinic connections exist. In our implementation we have assumed the existence of a Hamiltonian first integral.

system with associated Hamiltonian function (see e.g. [27])

$$H(x,y,p_x,p_y)=\frac{1}{2}(p_x^2+p_y^2)-xp_y+yp_x-\frac{1-\mu}{r_1}-\frac{\mu}{r_2}, \tag{1}$$

where $r_1=\sqrt{(x-\mu)^2+y^2}$ and $r_2=\sqrt{(x-\mu+1)^2+y^2}$. From now on, the value of the Hamiltonian on each orbit will be referred as the *energy*, denoted by h. We recall that the system of differential equations satisfies the well known symmetry

$$(t,x,y,p_x,p_y)\longrightarrow(-t,x,-y,-p_x,p_y). \tag{2}$$

This implies that, for each solution, there also exists another one, which is seen as symmetric with respect to $y=0$ in configuration space.

We also recall that the RTBP has five equilibrium points: the collinear points, L_1, L_2, and L_3, situated on the line containing the primaries at x_{L_i}, $i=1,2,3$, with $x_{L_2}\leq\mu-1\leq x_{L_1}\leq\mu\leq x_{L_3}$, and the equilateral ones, L_4 and L_5, both forming an equilateral triangle with the two primaries. We denote h_i the value of the energy at the equilibrium point L_i, $i=1,\ldots,5$.

We focus our attention on the dynamics of the RTBP around the collinear equilibrium points. It is well known [27] that, if we write the differential equations associated to (1) as

$$\dot{z}=X_H(z),$$

then Spec $DX_H(L_i)=\{\pm i\omega,\pm\lambda\}$, with $\omega,\lambda>0$, so the equilibrium point L_i, $i=1,2,3$, is a center×saddle point and Lyapunov's center theorem applies (see e.g. [24]). Thus, each equilibrium point gives rise to a one–parametric family of periodic orbits, spanning a 2D manifold tangent to real and imaginary parts of the eigenvectors of eigenvalues $\pm i\omega$ at the equilibrium point. This family is known as Lyapunov family of periodic orbits (LPO), and, close to the equilibrium point, it can be parametrized by the energy.

Since the equilibrium point is hyperbolic, the Lyapunov family inherits hyperbolicity and therefore the periodic orbits have unstable and stable manifolds. These manifolds are immersed cylinders $\mathbb{R}\times S^1$. Geometrically, they can be viewed as two dimensional "tubes" approaching (forwards and backwards in time) the periodic orbit (see, for example, Fig. 3 where the projection of the branches of the manifolds in the configuration space is shown). These unstable and stable manifolds can intersect, giving rise to homoclinic connections of the LPO.

2.2. Numerical methodology

A simple, general strategy to state the computation of a homoclinic connection as a zero–finding problem is the following. Let X be a hyperbolic p.o. with stable and unstable directions given by one–dimensional real eigenspaces of its monodromy matrix (it could also have central part or additional hyperbolic directions). Assume we have parametrizations of the manifolds $\psi^s(\theta,\xi)$, $\psi^u(\theta,\xi)$, where θ is an angle and $\xi\in\mathbb{R}$ is such that the parametrizations describe the p.o. for $\xi=0$ and the different branches of the manifolds for $\xi>0$ and $\xi<0$ (actual expressions are given below). Let $\Sigma=\{g(z)=0\}$

be a hypersurface known to be intersected by the manifold tubes, and consider two associated Poincaré maps: P_Σ^+, which propagates the flow forward in time until the next intersection with Σ, and P_Σ^-, which does the same backward in time. Choose values ξ_0^u, ξ_0^s, with $|\xi_0^u|, |\xi_0^s|$ small, and consider the function

$$F(\theta^u, \theta^s) = P_\Sigma^+(\psi^u(\theta^u, \xi_0^u)) - P_\Sigma^-(\psi^s(\theta^s, \xi_0^s)). \tag{3}$$

The values of (θ^u, θ^s) for which $F(\theta^u, \theta^s)$ is zero correspond to a homoclinic connection.

The function F and its differential DF can be numerically evaluated by numerical integration of $\dot{z} = X_H(z)$ and its first variational equations, so Newton's method can be used to find roots of F. Initial conditions for the Newton iteration can be found graphically by plotting the section of the tubes with Σ, that is, $\{P_\Sigma^+(\psi^u(\theta, \xi_0^u))\}_{\theta\in[0,2\pi)}$ and $\{P_\Sigma^-(\psi^s(\theta, \xi_0^s))\}_{\theta\in[0,2\pi)}$, as in Fig. 4. Each common point of these two sets corresponds to a zero of F.

Theoretically, the section Σ that defines the P_Σ^+ and P_Σ^- maps is defined locally, in a neighborhood of the intersection of the manifold tubes. In practice, it is more convenient to work with global sections defined by an implicit equation $\{g(z) = 0\}$ (actually, in all the computations of Sect. 3 we have used just hyperplanes of the form coordinate = constant). It may happen then, that the first cut with the section is not the one we are interested in. For instance, in Fig. 6, in order to match in $\Sigma = \{x = 0\}$ the first cut of the unstable manifold with the stable manifold, we need to consider the sixth cut of the stable manifold with Σ. In Sect. 3, notation will be introduced in order to deal with this issue.

The actual formula we have used for $\psi^u(\theta, \xi)$ is

$$\psi^u(\theta, \xi) = \phi_{\frac{\theta}{2\pi}T}(z_0) + \xi(\Lambda^u)^{-\theta/(2\pi)} D\phi_{\frac{\theta}{2\pi}T}(z_0) v_0^u, \tag{4}$$

where $\phi_t(z)$ is the time–t flow of the RTBP, z_0 is an initial condition of the p.o., T is its period ($\phi_T(z_0) = z_0$), v^u is an eigenvector of the monodromy matrix $D\phi_T(z_0)$ corresponding to the unstable manifold, and Λ^u is the corresponding eigenvalue. An analogous expression has been used for the stable manifold. Note that we are using the linear approximation. A first-order Taylor expansion shows that, for bounded $|t|$,

$$\phi_t(\psi(\theta, \xi)) = \psi(\theta + t\omega, e^{t\lambda}\xi) + O(\xi^2), \tag{5}$$

for $\psi = \psi^{u/s}, \omega = 2\pi/T$, $\lambda = (\omega \ln \Lambda)/(2\pi)$.§ Therefore, the manifold parametrized by $\psi(\theta, \xi)$ is invariant by the flow except for a quadratic term in ξ. Since we use double precision, in all the computations presented in Sect. 3 we have taken $|\xi|$ of the order of 10^{-6}.

The automatic continuation of families of homoclinic connections of p.o. by a predictor–corrector method [2] could be done letting z_0 free in $F(\theta^u, \theta^s) = 0$ and considering $v_0^u = v_0^u(z_0)$, $\Lambda^u = \Lambda^u(z_0)$, etc. However, it is difficult to evaluate the derivatives of eigenvalues and eigenvectors with respect to z_0 when they are computed

§ For $\Lambda < 0$, a real Floquet change is not possible. In such a case, we can consider the p.o. $2T$–periodic and work with $D\phi_T(z_0)^2 = D\phi_{2T}(z_0)$, which will have $\Lambda^2 > 0$ as corresponding eigenvalue. This has never happened in the computations of Sect. 3.

by a general–purpose numerical method (as implemented in linear algebra packages such as LAPACK [3]). This difficulty is avoided by adding the eigenvector condition to the system of equations, plus a normalization equation in order to have local uniqueness.

In order to state the system of equations we have used, consider $h \in \mathbb{R}$ an energy level, $z \in \mathbb{R}^4$ an initial condition of a p.o., T its period, $\Lambda^u, \Lambda^s \in \operatorname{Spec} D\phi_T(z)$, with $\Lambda^u > 1$ and $0 < \Lambda^s < 1$, v^u, v^s corresponding eigenvectors of $D\phi_T(z)$, θ^u, θ^s starting phases on the linear approximation of the unstable and stable manifolds, respectively, and $T^u, T^s \in \mathbb{R}$ the integration times required to intersect the section Σ from the starting points $\psi^u(\theta^u, \xi_0^u), \psi^s(\theta^s, \xi_0^s)$. Note that the introduction of these times avoids the need to take into account the number of cuts with the sections, which would have been necessary if we had considered Poincaré maps explicitly, as in the function F previously considered. Consider also $g_1 : \mathbb{R}^4 \longrightarrow \mathbb{R}$ a function defining a Poincaré section for the periodic orbit, and $g_2 : \mathbb{R}^4 \longrightarrow \mathbb{R}$ a function defining the Poincaré section to match the manifolds, this is, $\Sigma = \{g_2(z) = 0\}$. The system of equations we have used for the continuation of homoclinic connections of p.o. is

$$\begin{aligned}
H(z) - h &= 0, & D\phi_T(z)v^s - \Lambda^s v^s &= 0,\\
g_1(z) &= 0, & \|v^s\|^2 - 1 &= 0,\\
\phi_T(z) - z &= 0, & g_2\Big(\phi_{T^u}(\psi^u(\theta^u, \xi_0^u))\Big) &= 0,\\
D\phi_T(z)v^u - \Lambda^u v^u &= 0, & g_2\Big(\phi_{T^s}(\psi^s(\theta^s, \xi_0^s))\Big) &= 0,\\
\|v^u\|^2 - 1 &= 0, & \phi_{T^u}(\psi^u(\theta^u, \xi_0^u)) - \phi_{T^s}(\psi^s(\theta^s, \xi_0^s)) &= 0,
\end{aligned} \tag{6}$$

where $|\xi_0^u|, |\xi_0^s|$ are kept fixed to a small value (usually 10^{-6}), and the unknowns are

$$h, z, T, \Lambda^u, v^u, \Lambda^s, v^s, \theta^u, T^u, \theta^s, T^s.$$

Here $T, T^u > 0$ and $T^s < 0$.

In our setting, the integration times T^u, T^s may become large (this is the case in Sect. 3.2). In order to avoid loss of precision, we have also used a multiple shooting version of (6). For that, we have added new points as unknowns, along the p.o., $z_1, \ldots, z_{m-1}$, along the unstable branch, $z_1^u, \ldots, z_{m^u-1}^u$, and along the stable one, $z_1^s, \ldots, z_{m^s-1}$. The corresponding matching equations have been added to system (6), namely

$$\begin{aligned}
\phi_{T_i}(z_i) - z_{i+1} &= 0, \qquad i = 0, \ldots, m-2,\\
\phi_{T_i^u}(z_i^u) - z_{i+1}^u &= 0, \qquad i = 0, \ldots, m^u - 2,\\
\phi_{T_i^s}(z_i^s) - z_{i+1}^s &= 0, \qquad i = 0, \ldots, m^s - 2,
\end{aligned}$$

with $z_0 = z$, $z_0^u = \psi^u(\theta^u, \xi_0^u)$, $z_0^s = \psi^s(\theta_s, \xi_0^s)$. An adaptive strategy has been used, in the sense that the number of points, m, m^u, m^s, and integration times, $\{T_i\}_i, \{T_i^u\}_i, \{T_i^s\}_i$, have been recomputed at each continuation step in order to have

$$\|D\phi_t(z_i)\|_\infty < M, \qquad 0 < t < T_i,$$

and analogous inequalities along the unstable and stable branches. M has been taken typically of the order of tens or hundreds.

In all the computations of the following Section, the system (6) (or its multiple shooting version) and their derivatives with respect to all the unknowns have been evaluated from numerical integration by a variable step Runge–Kutta–Felbergh method of orders 7 and 8 of the RTBP equations, together with its first and second variationals. For that, a routine evaluating the augmented system of the RTBP equations including 1st and 2nd variationals has been written.‖ ¶ The tolerance of the RKF method used has been 10^{-14}. The absolute tolerances used to stop Newton iterates in the solution of either system (6) or its multiple shooting version have ranged from 10^{-10} to 10^{-12}.

Note also that, both in the single and multiple shooting cases, the system is over–determined and rank deficient. For instance, one of the equations including g_2 can be eliminated (it follows from the other equation including g_2 and the last one). An additional redundancy is that the equation $g_1(z) = 0$ allows to eliminate one of the equations in $\phi_T(z) - z = 0$. The reason for these redundancies follows from numerical experience, and its goal is to accelerate the convergence of Newton's method. Redundancy and rank–deficiency can be coped with by using the minimum–norm least–squares (LS) solution for the linear system that gives the Newton correction. Although redundant equations could be eliminated before each Newton iteration, their detection would need a linear analysis which is done automatically by the minimum–norm LS strategy at negligible computational cost. In our implementation, this solution has been computed using QR decomposition with column pivoting. For more details, see [17, 25].

As mentioned in the Introduction, the system of equations in Eq. (6) is not specific to the RTBP but is valid for any Hamiltonian system. With minor modifications, it would allow to continue heteroclinic connections of p.o.

3. Numerical results

This section is devoted to the presentation of numerical results on the computation of families of homoclinic connections of Lyapunov periodic orbits around the collinear points of the planar RTBP with the methodology presented in the previous section. In order to find homoclinic connections in the $L_{1,2}$ cases, only the first intersection of the manifold tubes with a surface of section will be considered. We will speak of *first–cut* homoclinics. Note that first–cut homoclinics are always primary, but the converse is not necessarily true, as we shall see. In the L_3 case, some additional cuts will be taken into account.

As shown in [8],[+] for the three collinear points, in the linear approximation of the

‖ Recent developments on general–purpose Taylor integrators using automatic differentiation [1, 19] will allow to obtain arbitrary–order derivatives of the flow just from the RTBP equations in the immediate future.

¶ The source code implementing the numerical methodology of this section is available upon request to the authors.

[+] Note that our convention for the ordering of the primaries on the x axis is reversed with respect to this reference.

flow around the point, and for a fixed energy level, a branch of the unstable manifold departs to the $\{x < x_{L_i}, y > 0\}$ region, and the other one departs to the $\{x > x_{L_i}, y < 0\}$ region (see Fig. 1). We will denote these branches as W^u_-, W^u_+, respectively. The application of symmetry (2) allows to obtain the branches W^s_-, W^s_+, entering from the $\{x < x_{L_i}, y < 0\}, \{x > x_{L_i}, y > 0\}$ regions, respectively. Following [8], we will call *transit orbits* the trajectories crossing the "bottleneck" region determined by the zero velocity curves (see Figs. 1, 2), going from the $\{x < x_{L_i}\}$ half space to the $\{x > x_{L_i}\}$ one or vice-versa, and *non–transit orbits* the ones bouncing back to any of the half-spaces. A necessary and sufficient condition for a trajectory approaching the LPO to be a transit orbit is to be inside one of the $W^s_\pm$ tubes, and analogously for an orbit departing from the LPO and the $W^u_\pm$ tubes. Although all these considerations correspond to the linear flow, we have observed the same qualitative behavior for the full flow in all the families of homoclinics computed, even for large energies.

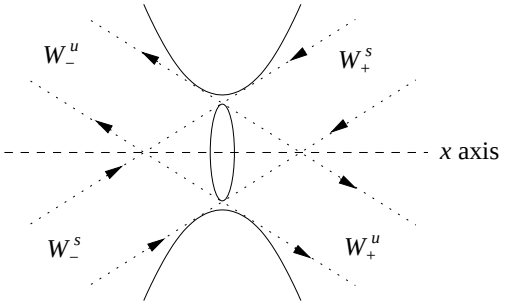

Figure 1. Sketch in configuration space of the naming convention for the manifold branches of an LPO. The solid curves represent the LPO and the zero–velocity curves (bounding the region of forbidden motion). The dotted lines represent the section with the xy plane of the manifold tubes. The arrows indicate direction of motion of trajectories following the manifold branches.

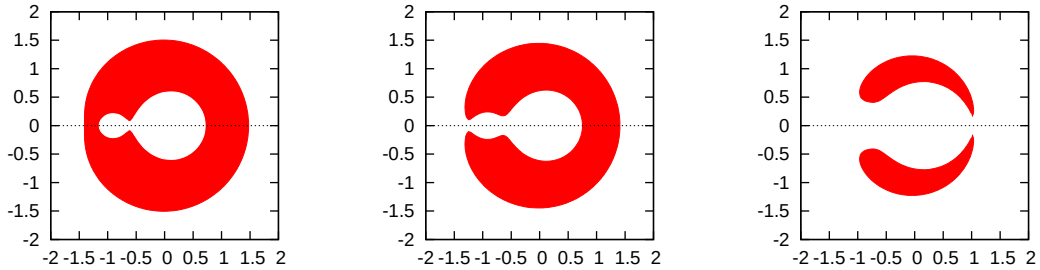

Figure 2. Hill's regions for $h_1 < h < h_2$ (left), $h_2 < h < h_3$ (center) and $h_3 < h < h_4 = h_5$ (right). Inside the filled regions, motion is not possible.

As mentioned before, in order to compute starting connections in each family, we will need to consider the number of cuts with the section Σ used to match the manifolds.

In what follows, we will denote the j–th cut of a branch of a manifold with a section Σ by $W^{s/u}_{\pm} \cap \Sigma^j$. We will say that there exists a homoclinic connection of type (j,k), $j,k \in \mathbb{Z}$, if

$$\left(W^u_{\operatorname{sign} j} \cap \Sigma^{|j|}\right) \cap \left(W^s_{\operatorname{sign} k} \cap \Sigma^{|k|}\right) \neq \emptyset. \tag{7}$$

Observe that all the pairs (j',k') such that $\operatorname{sign} j = \operatorname{sign} j'$, $\operatorname{sign} k = \operatorname{sign} k'$, $|j|+|k| = |j'|+|k'|$ give the same homoclinic connection as the pair (j,k).

Throughout this Section, in some figures where the projection of orbits or invariant manifolds in configuration space is shown, we have included the horizontal line $y=0$ (dotted line in the plots) that contains the primaries for greater clarity. Blue and red indicate that the piece of orbit or the set of points shown belongs to the stable and unstable manifold respectively.

3.1. Homoclinic connections to Lyapunov orbits around L_1 and L_2

In this Section, the mass parameter is fixed to the Earth–Moon mass ratio, $\mu_{EM} = 0.012150585609624042$. By numerically propagating the manifolds of LPO, it is seen that

- In the L_1 case, the $W^{u/s}_+$ tubes go around the large primary (Earth), and the $W^{u/s}_-$ go around the small one (Moon).
- In the L_2 case, the $W^{u/s}_+$ tubes go around the small primary, whereas the $W^{u/s}_-$ tubes exit the Hill region and go around the region of forbidden motion, surrounding both primaries.

Due to the topology of the region of forbidden motion (see Fig. 2 left, middle), first–cut homoclinics will be found by matching either the $W^{u/s}_+$ branches or the $W^{u/s}_-$ ones. We will present the corresponding results grouped in homoclinics surrounding the Moon and homoclinics surrounding either the Earth or both primaries.

3.1.1. Homoclinics to LPO surrounding the Moon From the behavior of the manifold branches, and using the section $\Sigma = \{x = \mu - 1\}$, the candidates to be first–cut homoclinics of LPO around the Moon are of type $(-1,-2)$ for L_1 (Fig. 3 left), and of type $(+1,+2)$, for L_2 (Fig. 3 right).

Since L_1 does not have a homoclinic connection of this type, neither do the corresponding LPO for energy levels close to h_1. As energy increases, the sets $W^u_- \cap \Sigma^1, W^s_- \cap \Sigma^2$ become tangent and, after that, they intersect at two points giving rise to two homoclinic connections (Fig. 4 left). We have labeled these connections as $\mathrm{Hm}_j, j = 1,2$, and we have followed them by the continuation procedure of Sect. 2.2. The corresponding characteristic curves are displayed in Fig. 5 left. The Hm_2 family goes to collision with the Moon very rapidly, whereas Hm_1 survives up to energies over -1.5.

The L_2 case is analogous: $W^u_+ \cap \Sigma^1, W^s_+ \cap \Sigma^2$ are disjoint at first, they become tangent and, for increasing energies, they display two intersection points (Fig. 4 right),

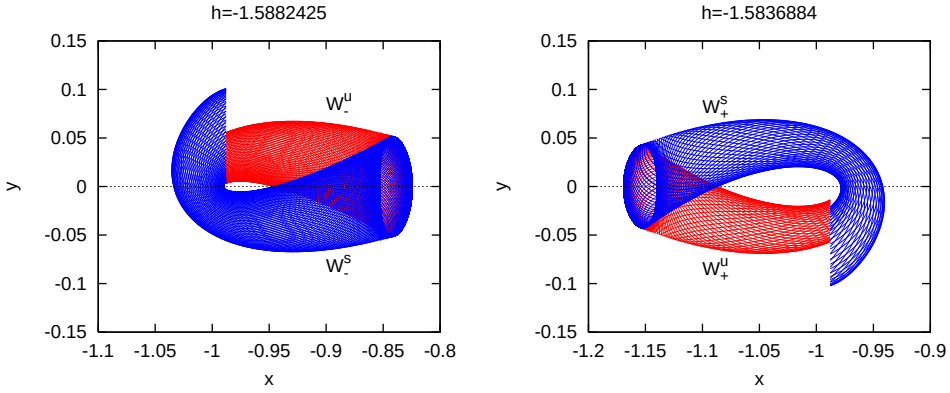

Figure 3. Projection in the configuration space of the invariant manifolds associated with a LPO around L_1 (left, branches $W_-^{u/s}$), and L_2 (right, branches $W_+^{u/s}$), up to a certain intersection with $\Sigma = \{x = \mu - 1\}$.

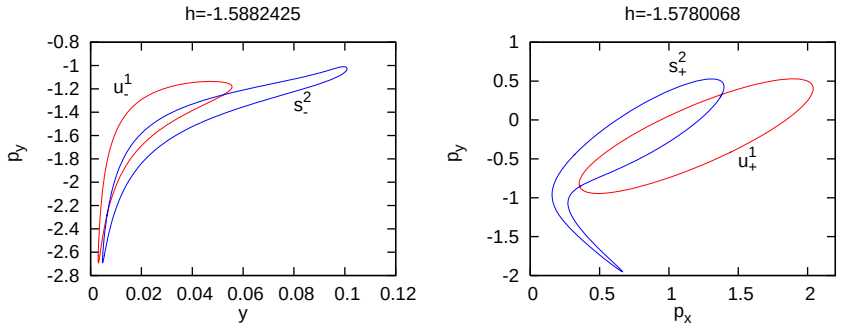

Figure 4. Left: for $\Sigma = \{x = \mu - 1\}$, sets $u_-^1 = W_-^u \cap \Sigma^1$ and $s_-^2 = W_-^s \cap \Sigma^2$ in the (y, p_y) plane for a LPO around L_1. Right: sets $u_+^1 = W_+^u \cap \Sigma^1$ and $s_+^2 = W_+^s \cap \Sigma^2$ in the (p_x, p_y) plane for a LPO around L_2 and the same section.

giving rise to two families of homoclinics, which we have labeled as $\mathrm{Hi}_j, j = 1, 2$. We have also followed them (Fig. 5 right).

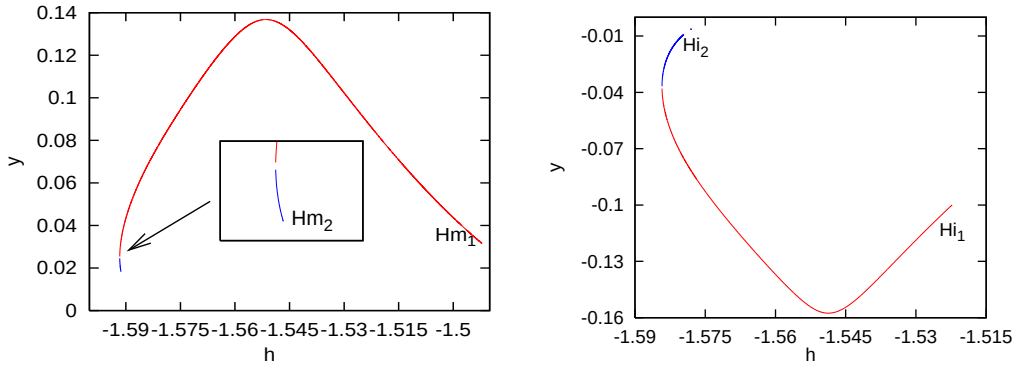

Figure 5. Characteristic curves in the (h, y) plane of families of homoclinic connections to LPO around L_1 (left) and L_2 (right) that surround the Moon (the y coordinates correspond to $\Sigma = \{x = \mu - 1\}$).

These computations are extensions of the computations in [6], where the $\mathrm{Hm}_j, \mathrm{Hi}_j$ families are computed using Lindstedt–Poincaré series, covering the energy range $[-1.5941705, -1.5686510]$ for the L_1 case, and $[-1.5860802, -1.5662235]$ for the L_2 case.

3.1.2. Homoclinics to LPO surrounding the Earth From the behavior of the manifold branches, and using the section $\Sigma = \{x = 0\}$, first–cut homoclinics of LPO surrounding the Earth have to be of type $(+1, +6)$ for L_1 (Fig. 6 left), and of type $(-1, -2)$ for L_2 (Fig. 6 right).

As before, L_1 does not have a homoclinic connection of this type, so neither do the corresponding LPO for energy levels close to h_1. As the energy increases, $W^u_+ \cap \Sigma^1$, $W^u_+ \cap \Sigma^6$ become tangent, two families of homoclinic connections appear, and, for larger energies, a new tangency gives rise to two new families so the sets $W^u_+ \cap \Sigma^1$, $W^u_+ \cap \Sigma^6$ have 4 common points (see Fig. 7 left). We have labeled the corresponding families He_j, $j = 1, 2, 3, 4$, and we followed them. Their characteristic curves are displayed in Fig. 9 left. Some homoclinics of these families are displayed in the top row of Fig. 10. For large energies they approach both primaries, and thus become interesting for cargo transportation applications in the Earth–Moon system [7].

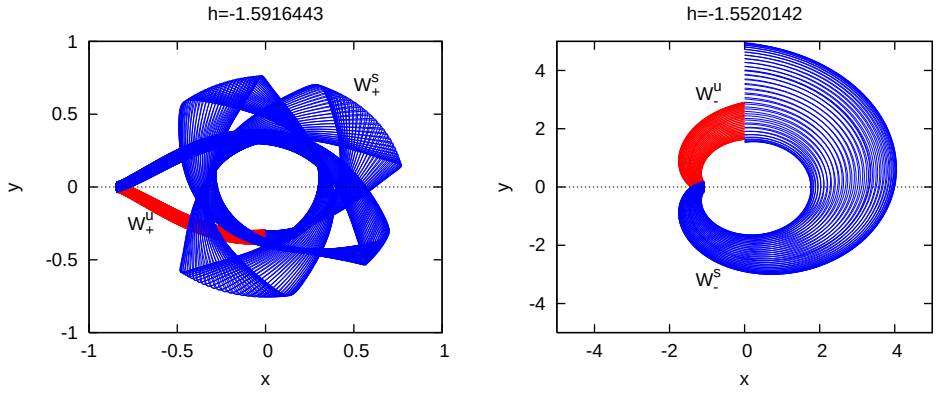

Figure 6. Invariant manifolds associated with a LPO around L_1 (left, branches $W^{u/s}_+$), and L_2 (right, branches $W^{u/s}_-$) up to a certain intersection with $\Sigma = \{x = 0\}$.

For the L_2 case, the situation is very much as before and we have first 2 families of homoclinics, and then 4 (see Fig. 7 right). However, as energy increases, $W^s_- \cap \Sigma^2$ spirals and generates new intersections with $W^u_- \cap \Sigma^1$ giving rise to additional families (see Fig. 8). We have followed up to 12 families Ho_i, $i = 1, \ldots, 12$, whose characteristic curves are displayed in Fig. 9 right. Some sample homoclinics of these families are displayed in the bottom row of Fig. 10.

3.2. Homoclinic connections of Lyapunov orbits around L_3

This subsection is devoted to families of homoclinics of LPO around L_3. As far as the authors know, these are the first computations of this kind done in the neighborhood of

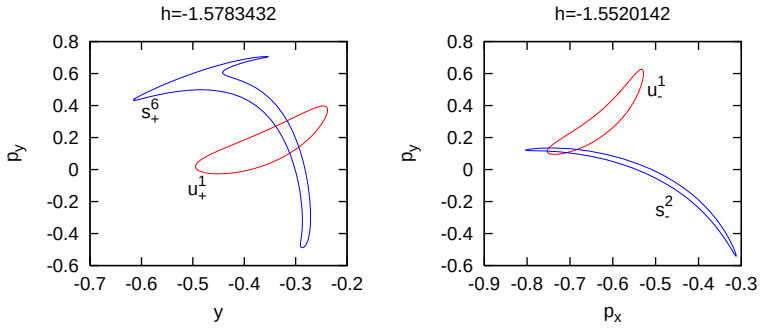

Figure 7. Left: for $\Sigma = \{x = 0\}$, sets $u_+^1 = W_+^u \cap \Sigma^1$ and $s_+^6 = W_+^s \cap \Sigma^6$ in the (y, p_y) plane for a LPO around L_1. Right: sets $u_-^1 = W_-^u \cap \Sigma^1$ and $s_-^2 = W_-^s \cap \Sigma^2$ in the (p_x, p_y) plane for a LPO around L_2 and the same section.

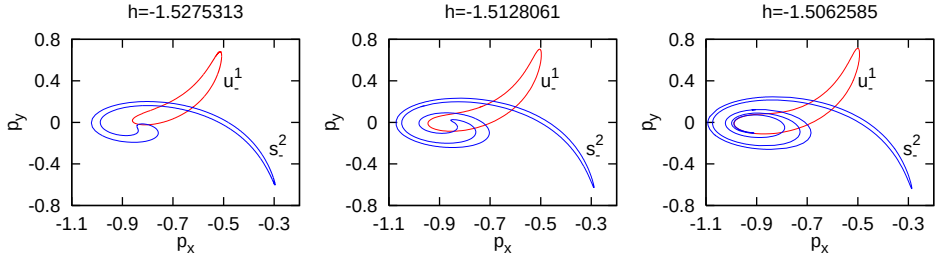

Figure 8. Curves $u_-^1 = W_-^u \cap \Sigma^1$ and $s_-^2 = W_-^s \cap \Sigma^2$ in the (p_x, p_y) plane, for the Lyapunov orbits around L_2 of the energies indicated and the section $\Sigma = \{x = 0\}$.

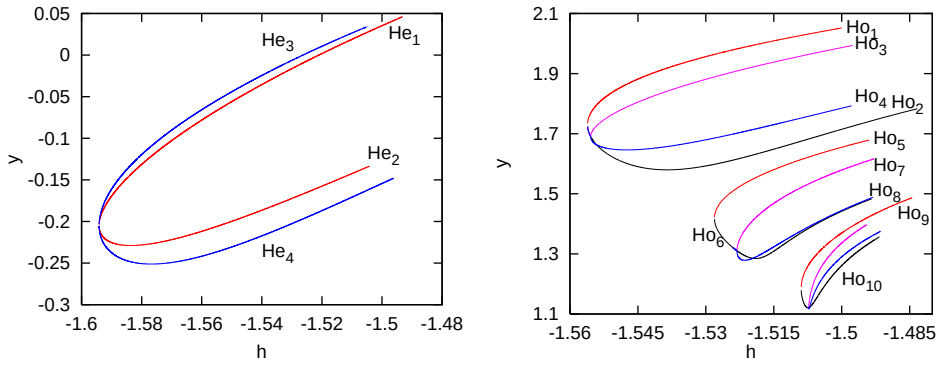

Figure 9. Characteristic curves in the (h, y) plane of families of homoclinic orbits that surround either the Earth only (left) or both the Earth and the Moon (right). The y coordinates correspond to the section $\{x = 0\}$.

L_3. For this reason, the exposition will be a little more detailed, and we will finish with some comments on the construction of trajectories with prescribed itineraries following different homoclinics of LPO. All the computations of this section correspond to the Sun–Jupiter mass parameter, $\mu = \mu_{SJ} = 9.53875 \times 10^{-4}$, in order to relate them to previous works on horseshoe motion [4, 5].

Locally, the branches of manifolds of LPO behave as in Fig. 1. When they go away from the LPO, they surround the islands of the region of forbidden motion (see

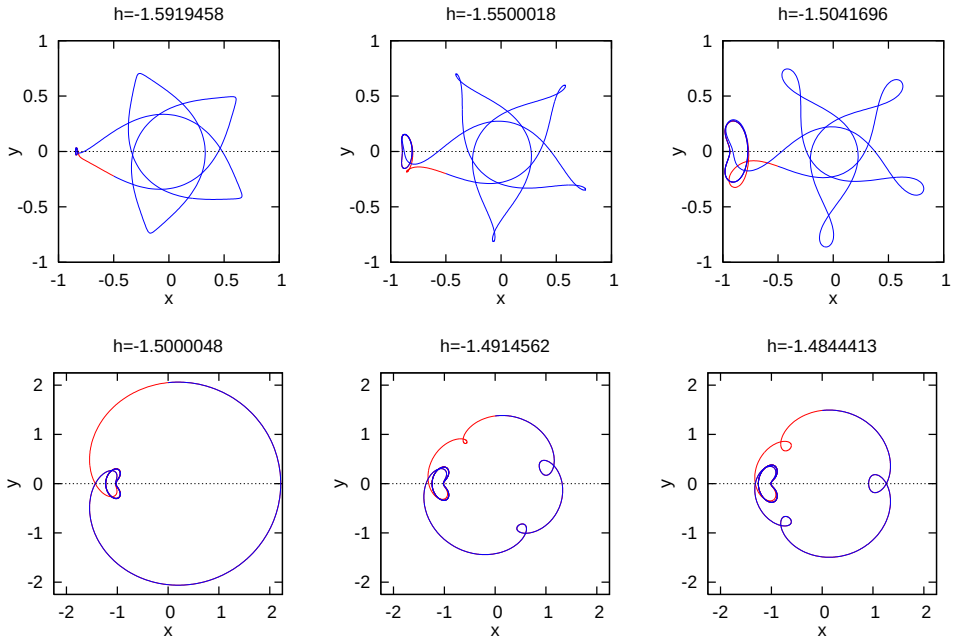

Figure 10. Projection in configuration space of homoclinic orbits to LPO around L_1 from the family He_1 (first row) and around L_2 from the family Hi_1 (second row).

Fig. 2 right). For that reason, and using the section $\Sigma = \{x = \mu - 1/2\}$, it seems reasonable to look for first–cut homoclinics of type $(+1, -2)$ (which, by symmetry (2), give homoclinics of type $(-2, +1)$). These homoclinics have the shape of a half horseshoe (see Fig. 11 left).

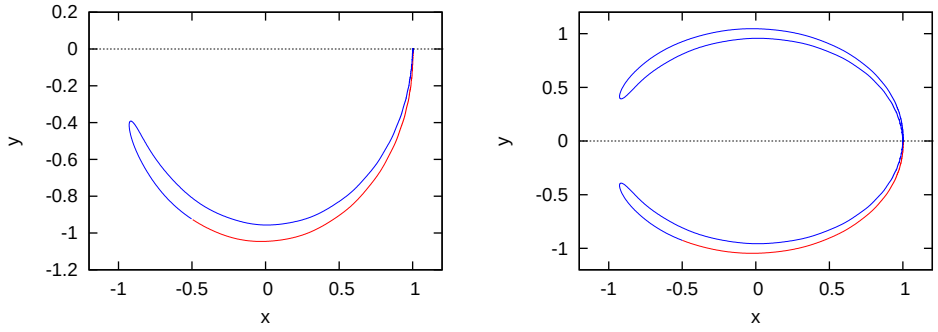

Figure 11. Left: (x, y) projection of a half horseshoe–shaped homoclinic orbit of type $(+1, -2)$ with respect to $\Sigma = \{x - 1/2\}$. Right: full horseshoe–shaped of type $(+1, +4)$ w.r.t. the same section.

The situation is very much like in the $L_{1,2}$ cases: the curves $W^u_+ \cap \Sigma^1$ and $W^s_- \cap \Sigma^2$ do not intersect at first (Fig. 12 left) and, after becoming tangent at energy $h_t := -1.5004766$, their intersection gives rise to two families of homoclinics (Fig. 12 right). We have labeled them as Hn_i, $i = 1, 2$, and we have also followed them. Their characteristic curves are shown in Fig. 13 left.

Before $W^u_+ \cap \Sigma^1$ intersects $W^s_- \cap \Sigma^2$, this is, for $h < h_t$, all the trajectories in $W^u_+ \cap \Sigma^1$

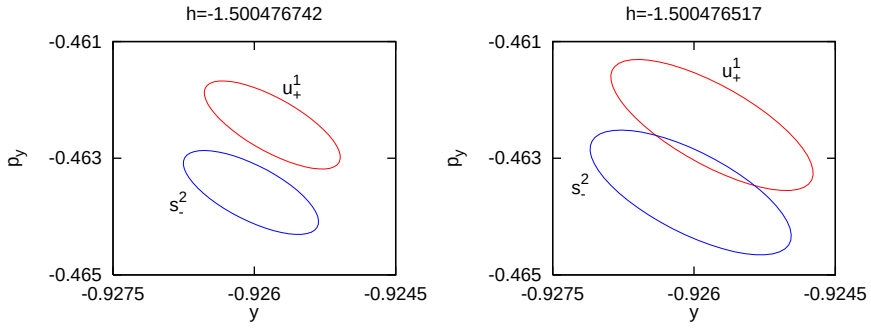

Figure 12. Projections in the (y, p_y) plane of the curves $u^1_+ = W^u_+ \cap \Sigma^1$ (red) and $s^2_- = W^s_- \cap \Sigma^2$ (blue) for a LPO around L_3 at the section $\Sigma = \{x = \mu - 1/2\}$, for the values of the energies indicated.

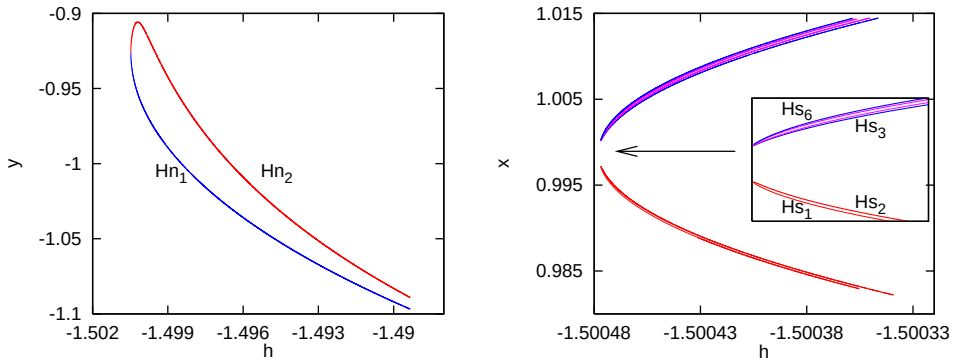

Figure 13. Left: characteristic curves of half horseshoe–shaped homoclinics of type $(+1, -2)$ w.r.t. $\Sigma = \{x = \mu - 1/2\}$. Right: characteristic curves of the full horseshoe–shaped homoclinics of type $(+1, +4)$ w.r.t. the same section. These last homoclinics are of type $(+2, +2)$ w.r.t. $\tilde{\Sigma} = \{y = 0\}$, which has been used for their computation. The x coordinates displayed correspond to $\tilde{\Sigma}$.

are non–transit. Therefore, after one turn around the island of the forbidden region in $\{y < 0\}$ (see Fig. 2 right), they avoid falling back to the LPO and perform a turn around the island in $\{y > 0\}$, opening the possibility for a symmetric, full horseshoe–shaped homoclinic of type $(+1, +4)$ (Fig. 11 right). It turns out that these kind of homoclinics appear before the $(+1, -2)$ do (see Fig. 14). When the $(+1, -2)$ homoclinics appear, the $(+1, +4)$ become secondary, so there must be an infinite number of them. This fact is reflected in that, as energy approaches h_t, the $W^s_+ \cap \Sigma^4$ section spirals and generates many new families, see Fig. 14. (Although not explored, this phenomenon also takes place in the $L_{1,2}$ cases, as in Fig. 8.) In spite of this complicated behavior, the procedure of Sect. 2.2 is able to follow any of the $(+1, +4)$ families to energies past h_t. Among these families, we have followed some of the symmetric ones, whose characteristic curves are displayed in Fig. 13 right.

A remarkable difference between the dynamics around L_1, L_2 and that of L_3 comes from the geometry of the manifolds tubes. Close to the equilibrium point, the orbits can be approximated by a two-body problem solution with period close to that of the small

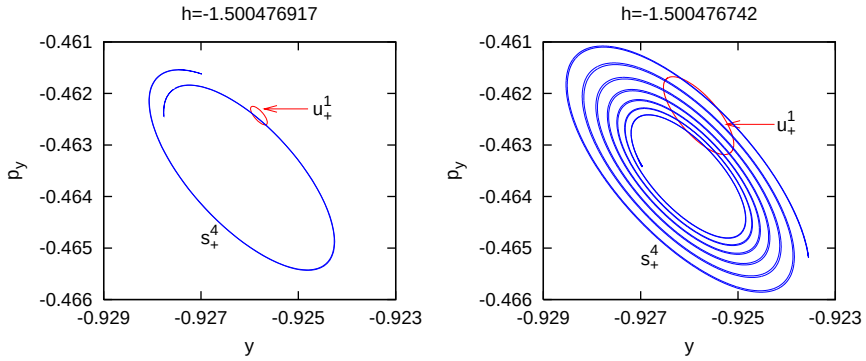

Figure 14. Using the section $\Sigma = \{x = \mu - 1/2\}$, (y, p_y) projection of the curves $u^1_+ = W^u_+ \cap \Sigma^1$ (red) and $s^4_+ = W^s_+ \cap \Sigma^4$ (blue), for the values of the energies indicated.

primary. This slow dynamics causes the orbits to perform loops in the rotating frame, which increase as the LPO becomes larger (see Fig. 15 and [5] for an analysis of the presence of loops in horseshoe motion from the $\mu = 0$ case). Small loops "straighten out" along the manifold, like in Fig. 15 left, and present no problems. But, as they become bigger, they eventually reach the surface of section (Fig. 15 right) and the $(\pm i, \pm j)$ classification of homoclinics stops making sense. This fact makes difficult to find the intersection sets defined in (7). This is not a problem for the continuation method of Sect. 2.2, because it does not make use of the number of cuts necessary in order to reach the section. However, in order to check for the appearance of new families of homoclinics, it is convenient to be able to have a clear representation of the section of the manifold tubes.

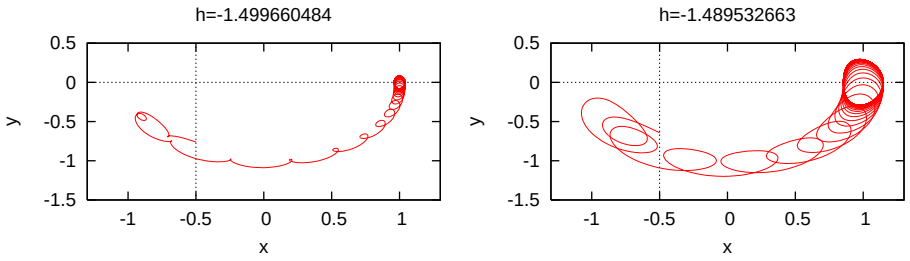

Figure 15. Projection in the (x, y) plane of two orbits of W^u_+ up to its second intersection with $\Sigma = \{x = \mu - 1/2\}$, plotted as a dotted line for clarity. As the energy increases, the loops reach a neighborhood of the section Σ.

A way to obtain these representations is by doing continuation of the equation

$$g(\psi(\theta, \xi)) = 0$$

with respect to (θ, ξ), where $\psi(\theta, \xi)$ is a parametrization of the invariant manifold tube ($|\xi|$ not being necessarily small), and the section is given by $\Sigma = \{g(z) = 0\}$, for $g : \mathbb{R}^4 \to \mathbb{R}$. A simple way to numerically evaluate such a parametrization is using the linear approximation and globalizing by numerical integration. Namely, for $|\xi|$ not

necessarily small, we can take

$$\psi(\theta,\xi) = \phi_{t^*}\Big(\psi(\theta - t^*\omega, e^{-t^*\lambda}\xi)\Big),$$

for t^* such that $|e^{-t^*\lambda}\xi|$ is small, ω, λ defined as in (5), and we can use (4) to evaluate ψ on the right–hand side of the previous equation.

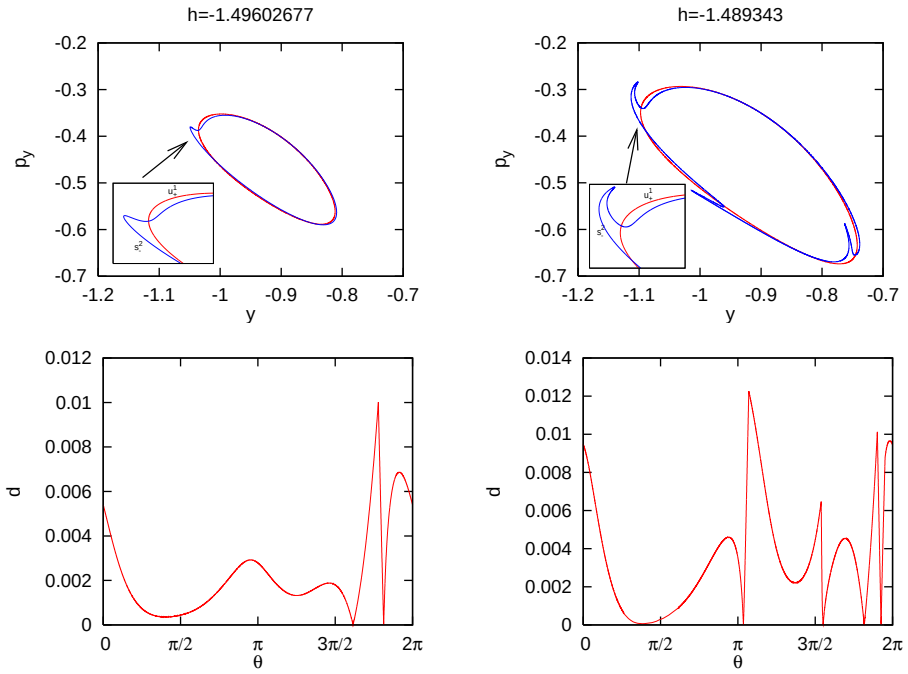

Figure 16. Top: for the energies indicated, (y, p_y) projection of curves $W^u_+ \cap \Sigma^1$ (red) and $W^s_- \cap \Sigma^2$ (blue). Bottom: for the energies of the top row, distance d of each point of the curve $W^u_+ \cap \Sigma^1$ to the curve $W^s_- \cap \Sigma^2$, which shows the number of intersections between them.

The sections of the manifold tubes of the top row of Fig. 16 have been computed in this way. They correspond to the $(+1, -2)$ homoclinics (Hn_i families) introduced above. These plots are useful to check for the appearance of new families. With this, special care has to be taken because visual inspection can be misleading, as is illustrated in Fig. 16. For energy $h = -1.49602677$, a graph of the distance of each point of the curve $W^u_+ \cap \Sigma^1$ to the curve $W^s_- \cap \Sigma^2$ (Fig. 16 bottom left) shows that in Fig. 16 top left there are only two intersections. For energy $h = -1.48934394$, the same kind of graph shows that in Fig. 16 top right there are 4 intersections, so two new families of homoclinics have appeared. We have not followed them.

3.3. The geometry of the manifold tubes

In this subsection we would like to make some comments on the geometry of the manifold tubes for the L_3 case, in order to investigate the possible generation of trajectories with prescribed itineraries. We would also like to illustrate graphically how the existence of a

primary homoclinic connection leads to the appearance of an infinite number of higher–order homoclinics. Similar studies for the L_1 and L_2 points can be found in previous works [13, 14, 20].

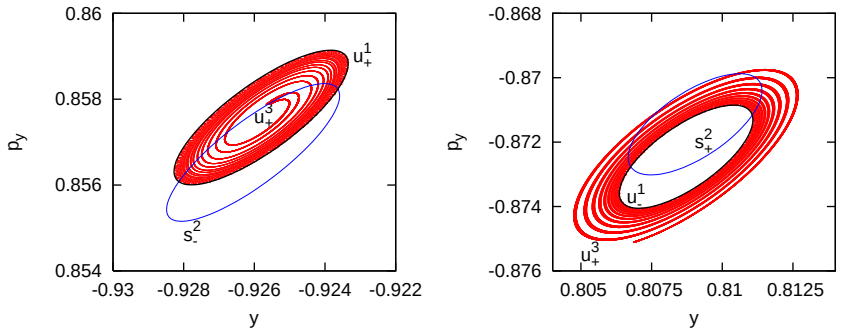

Figure 17. For $h = -1.50047477$. Left: (y, p_x) projection of the curves $s^2_- = W^s_- \cap \Sigma^2$ (blue), $u^1_+ = W^u_+ \cap \Sigma^1$ (black), and the component with $y < 0$ of the curve $u^3_+ = W^u_+ \cap \Sigma^3$ (red). Right: (y, p_x) projection of the curves $s^2_+ = W^s_+ \cap \Sigma^2$ (blue), $u^1_- = W^u_- \cap \Sigma^1$ (black), and the component with $y > 0$ of the curve $u^3_+ = W^u_+ \cap \Sigma^3$ (red).

For the energy level $h = -1.50047477$ and section $\Sigma = \{x = \mu - 1/2\}$, consider the curves $W^u_+ \cap \Sigma^1$ and $W^s_- \cap \Sigma^2$, which are plotted in Fig. 17 left in black and blue colors respectively. The points inside the black curve correspond to transit trajectories backward in time, meaning that, when propagated backwards, at the close approach with the LPO they exit through the W^s_- branch and complete a turn around the island of forbidden motion in $\{y < 0\}$. The points outside the black curve in Fig. 17 left are non–transit trajectories backward in time, meaning that, when propagated backwards, at the close passage to the LPO they exit through the W^s_+ branch and perform a revolution around the island of forbidden motion in $\{y > 0\}$. Examples of such transit and non–transit trajectories are given in Fig. 18. A similar description holds for transit and non–transit trajectories forward in time with respect to the (blue) curve $W^s_- \cap \Sigma^2$ in Fig. 17 left. As previously mentioned, the proofs of these facts can be found in [8].

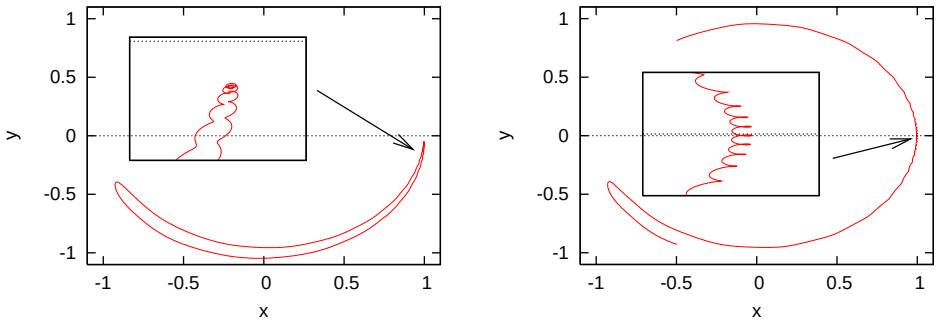

Figure 18. For $h = -1.50047477$, examples of a transit (left) and non–transit (right) orbits in the neighborhood of L_3. The starting points have been taken in $\{x = \mu - 1/2, y < 0\}$.

Now consider the curve $W^u_+ \cap \Sigma^3$ (red curve in Fig. 17 left), which is the second section with Σ forward in time of the points of $W^u_+ \cap \Sigma^1$ (black curve). The curve $W^u_+ \cap \Sigma^1$ is divided by the $W^s_- \cap \Sigma^2$ (blue curve) in two segments: the one inside $W^s_- \cap \Sigma^2$, which we denote as A, and the one outside, which we will call B. The points in the A segment correspond to transit orbits forward in time, so they stay in the $\{y < 0\}$ for the next 2 cuts with Σ, and give the red curve in Fig. 17 left (see also Fig. 18 left). The points in the B segment correspond to non–transit orbits forward in time, so they have the next two cuts with Σ in $\{y > 0\}$, giving the red curve in Fig. 17 right (see also Fig. 18 right). In this way, $W^u_+ \cap \Sigma^3$ has two components, that accumulate to the section of the manifold branch that they follow after the close passage to the LPO. Note that, in the first case, they accumulate inside $W^u_+ \cap \Sigma^1$, since they are transit orbits backward in time. In the second case they are non–transit, so they accumulate outside $W^u_- \cap \Sigma^1$.

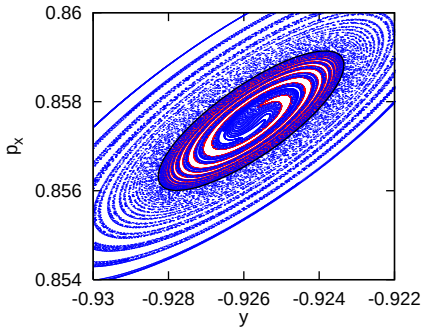

Figure 19. For $h = -1.50047477$, (y, p_x) projection of curves $W^u_+ \cap \Sigma^1$ (black), $W^u_+ \cap \Sigma^3$ (red), and $W^u_+ \cap \Sigma^5$ (blue).

This scheme can be iterated. In Fig. 19, we have added $W^u_+ \cap \Sigma^5$ (in blue) to the curves in Fig. 17 left. All the points inside $W^u_+ \cap \Sigma^1$ correspond to transit trajectories backward in time. In the second close passage to the LPO (backward in time), they may be either transit, non–transit, or belong to $W^u_+ \cap \Sigma^3$, in which case they tend to the LPO. Therefore, $W^u_+ \cap \Sigma^3$ separates transit from non–transit points in the second LPO passage. Since the points of $W^u_+ \cap \Sigma^5$ are transit in the second LPO passage, they determine the transit component. In this way, the position of points with respect to the $W^u_+ \cap \Sigma^3$ curve determine their past history up to two approaches to the LPO. A similar analysis can be done outside the curve $W^u_+ \cap \Sigma^1$, and also forward in time, with respect to the curve $W^s_- \cap \Sigma^2$. The consideration of higher numbers of cuts of the manifolds would allow to determine the behavior of further close passages to the LPO, either forward or backward in time.

A rigorous study using symbolic dynamics would allow to show the existence of orbits with prescribed itineraries. Studies of this kind have been done in [13, 14, 21] for LPO around the L_1 and L_2 points. The difference between L_3 and the previous points is that, instead of prescribing itineraries between the interior and exterior regions of the zero velocity curve, here we would prescribe itineraries alternating between the $\{y > 0\}$ and $\{y < 0\}$ regions. Among these trajectories, we could find periodic orbits

with half or full horseshoe shape, visiting the upper and lower half–spaces as many times as desired.

4. Acknowledgements

The authors would like to thank the referees for the careful reading they did of the first manuscript and their comments, which helped to improve this final version. E. Barrabés and J. M. Mondelo are partially supported by the MCyT/FEDER grants BFM2003-09504-C02-01 and MTM2006-05849/Consolider. J. M. Mondelo is also supported by the MCyT/FEDER grant MTM2008-01486 and the Catalan grant 2009SGR410. M. Ollé is partially supported by the MCyT/FEDER grant MTM2009-06973 and the Catalan grant 2009SGR-859.

5. References

[1] A. Abad, R. Barrio, F. Blesa, and M. Rodríguez, *TIDES: a Taylor Integrator for Differential Equations*, Preprint, 2009.

[2] E. L. Allgower and K. Georg, *Numerical continuation methods*, vol. 13 of Springer Series in Computational Mathematics, Springer-Verlag, Berlin, 1990. An introduction.

[3] E. Anderson, Z. Bai, C. Bischof, S. Blackford, S. J. Demmel, J. Dongarra, J. D. Croz, A. Greenbaum, S. Hammarling, A. McKenney, and D. Sorensen, *LAPACK Users' Guide*, SIAM, third ed., 1999.

[4] E. Barrabés and S. Mikkola, *Families of periodic horseshoe orbits in the restricted three-body problem*, Astronomy & Astrophysics, 432 (2005), pp. 1115–1129.

[5] E. Barrabés and M. Ollé, *Invariant manifolds of L_3 and horseshoe motion in the restricted three-body problem*, Nonlinearity, 19 (2006), pp. 2065–2089.

[6] E. Canalias and J. J. Masdemont, *Homoclinic and heteroclinic transfer trajectories between planar Lyapunov orbits in the sun-earth and earth-moon systems*, Discrete Contin. Dyn. Syst., 14 (2006), pp. 261–279.

[7] J. Casoliva, J. M. Mondelo, B. F. Villac, K. O. Mease, E. Barrabés, M. Ollé, *Families of Cycler Trajectories in the Earth–Moon system*, Paper AIAA 2008–6434, AIAA/AAS Astrodynamics Specialist Conference and Exhibit, August 2008, Honolulu, Hawai.

[8] C. C. Conley, *Low energy transit orbits in the restricted three-body problem*, SIAM J. Appl. Math., 16 (1968), pp. 732–746.

[9] M. Connors, P. Chodas, S. Mikkola, P. Wiegert, C. Veillet, and K. Innanen, *Discovery of an asteroid and quasi-satellite in an earth-like horseshoe orbit*, Meteoritics & Planetary Science, 37 (2002), pp. 1435–1441.

[10] D. W. Dunham and R. W. Farquhar, *Libration point missions, 1978–2002*, in Libration Point Orbits and Applications, G. Gómez, M. W. Lo, and J. J. Masdemont, eds., 2003.

[11] E. J. Doedel, B. W. Kooi, G. A. K. Van Voorn, and Yu. A. Kuznetsov, *Continuation of connecting orbits in 3D-ODEs: (II) Cycle-to-cycle connections*, International Journal of Bifurcation and Chaos, 19 (2009), pp. 159–169.

[12] E. J. Doedel, A. R. Champneys, T. F. Fairgrieve, and Y. A. Kuznetsov, *Auto97: Continuation and bifurcation software for ordinary differential equations*, tech. report, Concordia University, Montreal, Canada, 1997.

[13] M. Gidea and J. J. Masdemont, *Geometry of homoclinic connections in a planar circular restricted three-body problem*, Internat. J. Bifur. Chaos Appl. Sci. Engrg., 17 (2007), pp. 1151–1169.

[14] G. Gómez, W. S. Koon, M. W. Lo, J. E. Marsden, J. Masdemont, and S. D. Ross, *Connecting orbits and invariant manifolds in the spatial Restricted Three-Body Problem*, Nonlinearity, 17 (2004), pp. 1571–1606.

[15] G. Gómez, M. Marcote, and J. M. Mondelo, *The invariant manifold structure of the spatial Hill's problem*, Dynamical Systems. An International Journal, 20 (2005), pp. 115–147.

[16] G. Gómez and J. J. Masdemont, *Some zero cost transfers between Libration Point orbits*, Advances in the Astronautical Sciences, 105 (2000), pp. 1199–1216.

[17] G. Gómez and J. M. Mondelo, *The dynamics around the collinear equilibrium points of the RTBP*, Phys. D, 157 (2001), pp. 283–321.

[18] K. C. Howell, B. T. Barden, R. S. Wilson, and M. W. Lo, *Trajectory design using a dynamical systems approach with application to GENESIS*, Advances in the Astronautical Sciences, 97 (1998), pp. 1665–1684.

[19] A. Jorba and M. Zou, *A package for the automatic generation of Taylor integrators for high order variational equations of ODEs*, International Conference on Scientific Computation and Differential Equations, Beijing, China, 2009.

[20] W. S. Koon, M. W. Lo, J. E. Marsden, and S. D. Ross, *Heteroclinic connections between periodic orbits and resonance transitions in celestial mechanics*, Chaos, 10 (2000), pp. 427–469.

[21] J. Llibre, R. Martínez, and C. Simó, *Tranversality of the invariant manifolds associated to the Lyapunov family of periodic orbits near L_2 in the restricted three-body problem*, J. Differential Equations, 58 (1985), pp. 104–156.

[22] J. Llibre and M. Ollé, *The motion of saturn coorbital satellites in the restricted three-body problem*, Astronomy and Astrophysics, 378 (2001), pp. 1087–1099.

[23] R. P. Mcgehee, *Some homoclinic orbits for the restricted three-body problem*, PhD thesis, University of Wisconsin, 1969.

[24] K. R. Meyer and G. R. Hall, *Introduction to Hamiltonian dynamical systems and the N-body problem*, vol. 90 of Applied Mathematical Sciences, Springer-Verlag, New York, 1992.

[25] J. M. Mondelo, *Contribution to the Study of Fourier Methods for Quasi-Periodic Functions and the Vicinity of the Collinear Libration Points*, PhD thesis, Universitat de Barcelona, 2001.

[26] J. S. Parker and M. W. Lo, *Shoot the moon 3D*, Advances in the Astronautical Sciences, 123 (2006), pp. 2067–2086.

[27] V. Szebehely, *Theory of Orbits. The Restricted Problem of Three Bodies.*, Academic Press, Inc., 1967.

[28] D. Wilczak and P. Zgliczyński, *Heteroclinic connections between periodic orbits in planar restricted circular three-body problem—a computer assisted proof*, Comm. Math. Phys., 234 (2003), pp. 37–75.

[29] ———, *Heteroclinic connections between periodic orbits in planar restricted circular three body problem. II*, Comm. Math. Phys., 259 (2005), pp. 561–576.